Electronic Supplementary Information (ESI) for "Symmetry-derived Structure Directing Agents for Two-dimensional Crystals of Arbitrary Colloids"

Nathan A. Mahynski*, Vincent K. Shen

*Chemical Sciences Division, National Institute of Standards and Technology, Gaithersburg, Maryland 20899-8320, USA. Tel: +1 301-975-6836; E-mail: nathan.mahynski@nist.gov

S1 Derivation of Ring Sequence from Wallpaper Group Diagrams

In what follows, we illustrate the derivation of ring sequence and shape from the wallpaper group diagrams in the International Tables for Crystallography, Volume A. [1] We point out that different ring shapes (fundamental domains) and therefore sequences are possible; these simply reflect our choices following previous work, [2, 3] which does not detract from the generality of our results. Figures S1–S5 all follow the same layout. Starting from the left, a wallpaper group diagram is shown; solid gray lines serve as visual aids but do not denote symmetry elements, whereas dashed lines indicate glide-mirror planes, solid black lines denote mirror planes, ovals represent 2-fold rotation centers, and regular n-polygons denote n-fold rotation centers. A single fundamental domain is highlighted, bounded by colored arrows and circles, on which a 5-bladed pinwheel motif is drawn to illustrate the operations of the group. Colored lines with arrows are used to denote symmetrically equivalent edges; identically colored circles also denote which corners are symmetrically equivalent, but the coloring schemes for edges and corners are not related to each other. The direction of an arrow is included to illustrate the relative direction that it matches another edge of the same color, but is chosen arbitrarily, and could, for example, be reversed. A 2-headed arrow denotes a 2-fold rotation at its center implying equivalence around its midpoint. This color-coded mapping of equivalent edges defines a fundamental polygon. [4, 5, 6, 7]

Next, the ring itself is drawn. This is the "middle" layer of our model in which symmetrically unique positions are given unique identities denoted by different colors. When angle potentials are added, corners develop and the energetically minimized ring is shown next. Edges corresponding to the fundamental domain drawn on the symmetry diagram are shown for reference. When the ring is deformed, as discussed further in Sec. S3.1, the equilibrium angles at different corners are increased or decreased by an amount related to ψ (defined therein). An energetically minimized ring following these adjustments is shown next, though we emphasize some fluctuations are possible since the ring is not perfectly rigid and is simulated at finite temperature. Finally, we illustrate those deformations with curved edges on the symmetry diagram for comparison. Recall that in our model: (1) mirrored edges cannot be deformed and remain straight, (2) an edge with a 2-fold rotation at its center becomes "wave-like", and (3) all other edges (translated, rotated about an end point, or which undergo glide reflection) are deflected and appear as half of such a wave (*cf.* Sec. S3.1). When deformations occur, the equilibrium angle of the corners may change; this change is a multiple of ψ and is indicated on the diagrams for each corner where they occur.

All such deformations to the candidate fundamental domain must respect the symmetry operations of the group while maintaining a minimal area; resulting restrictions on the shape and size are given in the captions and are discussed more in Refs. [2, 3] for the choices made here, and more generally in Refs. [1, 7]. Once the domain is chosen, the symmetry operations determine which points along different edges are symmetrically equivalent. Folding or bending the plane to align matching points results in the corresponding orbifold. [8] Here we label edges with a fixed number of beads, N_1 and N_2, that define a parallelogram from which our fundamental domain has been derived, which we take as inputs along with an angle, γ, between them. [2, 3]

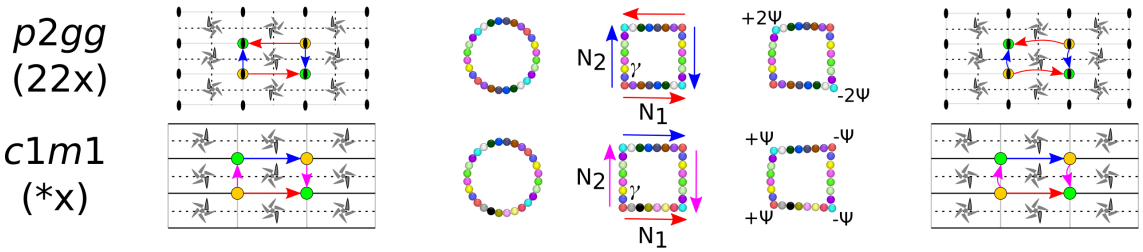

Figure S1: Summary of row 1 groups from the main text. For both groups $p2gg$ and $c1m1$, the fundamental domain chosen is a rectangle with $\gamma = \pi/2$. The angle ψ is defined in Sec. S3.1.

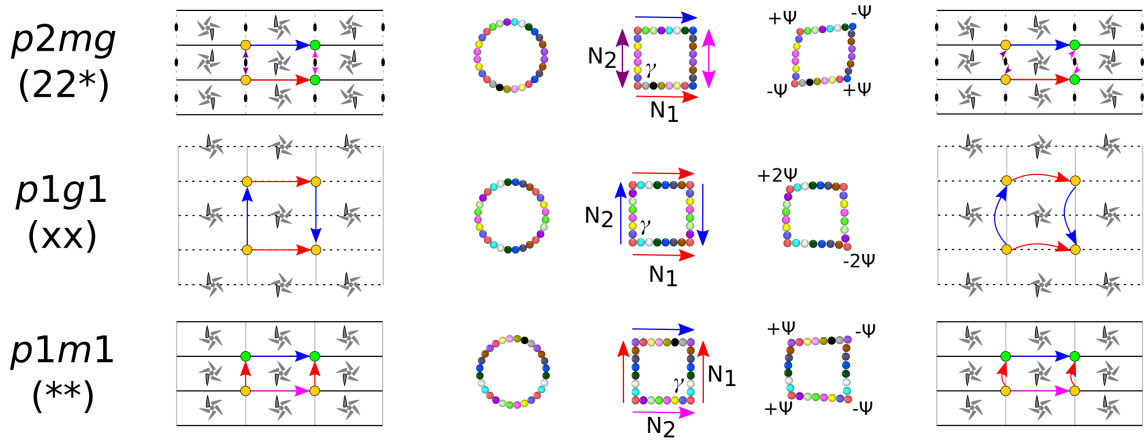

Figure S2: Summary of row 2 groups from the main text. For all these groups, the fundamental domain chosen is a rectangle with $\gamma = \pi/2$. The angle ψ is defined in Sec. S3.1.

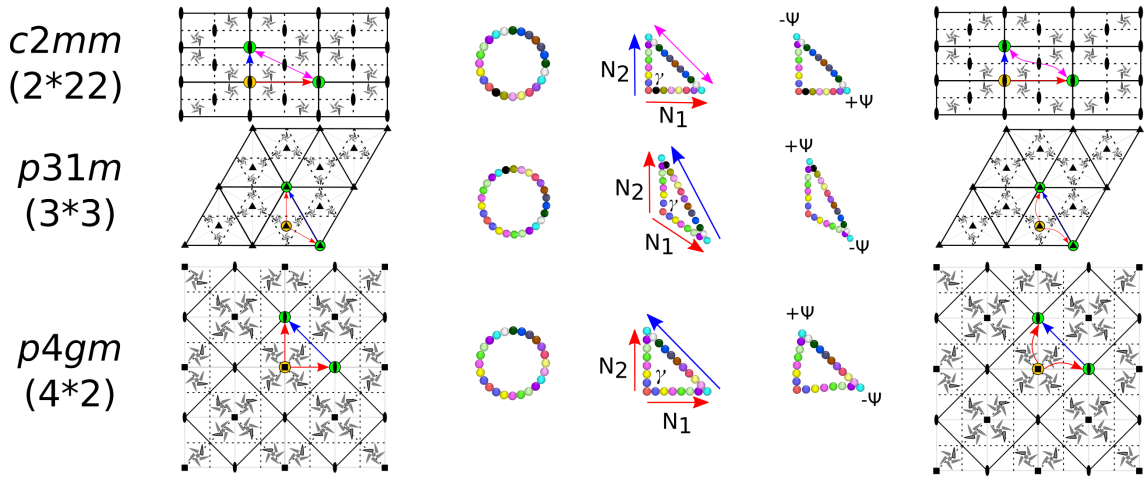

Figure S3: Summary of row 3 groups from the main text. These groups are formed from a region bounded by intersecting mirror planes containing a center of rotation, hence the A*{b} orbifold pattern, where A is an integer and {b} is a set of integers. For the $c2mm$ group, the fundamental domain chosen is a right triangle ($\gamma = \pi/2$) with no restrictions on the relative lengths of its sides; however, for $p31m$, $N_1 = N_2$ and $\gamma = 2\pi/3$ and for $p4gm$, $N_1 = N_2$ and $\gamma = \pi/2$, are selected.

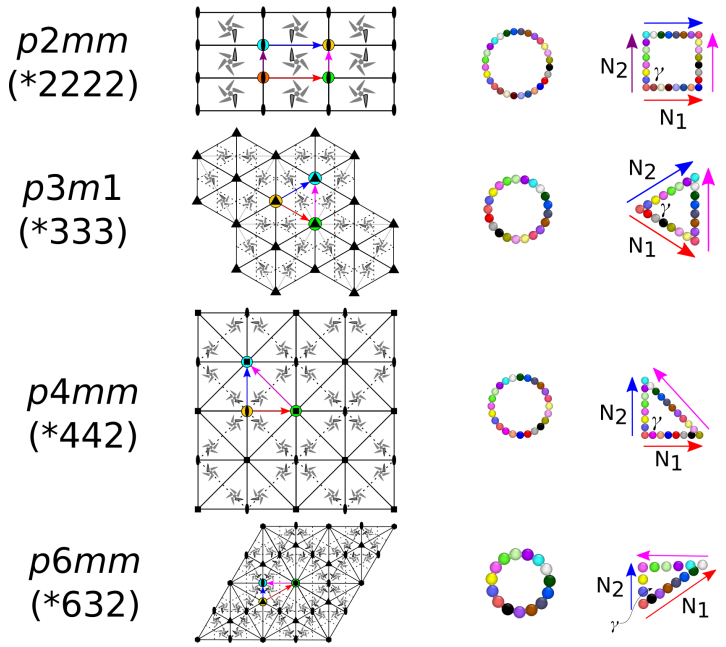

Figure S4: Summary of row 4 groups from main text. These groups are formed exclusively as a result of intersecting mirror planes, hence the *{a} orbifold pattern, where a is a set of integers. Thus, we refer to these groups as kaleidoscopes. For the $p2mm$ group, the fundamental domain is a rectangle with $\gamma = \pi/2$; whereas for $p3m1$, $N_1 = N_2$ and $\gamma = \pi/3$ (equilateral triangle), for $p4mm$, $N_1 = N_2$ and $\gamma = \pi/2$ (right isosceles triangle), and for $p6mm$, $\gamma = \pi/3$ and $N_2 = N_1/2$ (right scalene triangle).

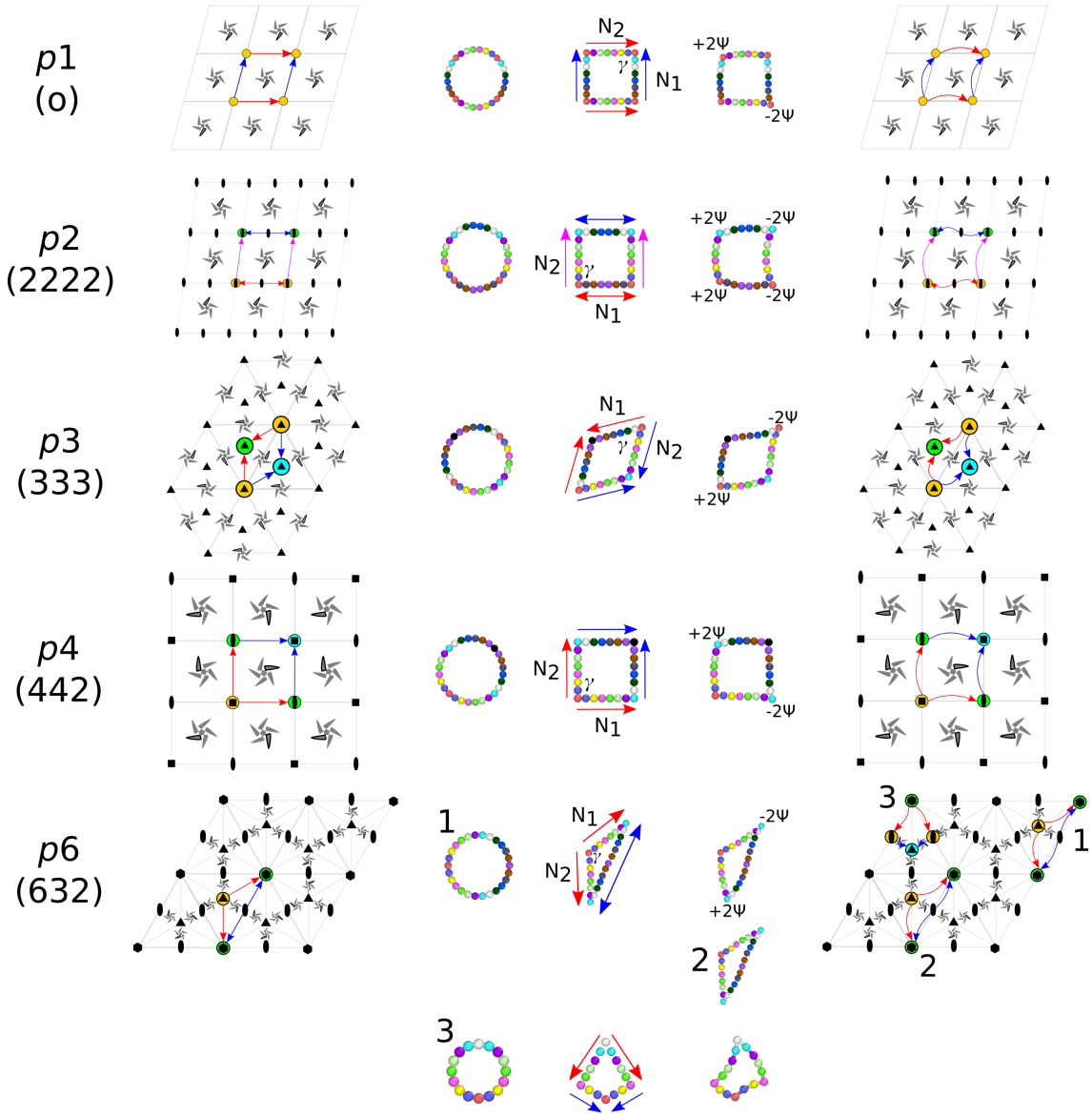

Figure S5: Summary of row 5 groups from the main text. These groups are formed exclusively as a result of rotations about an axis normal to the plane, hence the {A} orbifold pattern. The mapping of one edge to another by a rotation operation makes the net sequence palindromic about that center of rotation, so we refer to these groups as palindromes; note that $p1$ is technically not palindromic since it contains no rotations. The fundamental domain chosen for both $p1$ and $p2$ is a parallelogram with no restrictions on the relative lengths of its sides or γ. For $p3$, the domain selected is a rhombus ($N_1 = N_2$) with $\gamma = \pi/3$ and for $p4$, the domain is a square ($N_1 = N_2$ and $\gamma = \pi/2$). We illustrate several different fundamental domains that can be chosen for $p6$. In the first two, an isosceles triangle is selected ($N_1 = N_2$, $\gamma = 2\pi/3$). In (1) the way the deformations are chosen causes a "pinch" point to occur at one acute vertex while the other is expanded. If the deformations are chosen differently, as in (2), these can be avoided leaving the corner angles unaffected; only the equilibrium angles along the edges are modified. Finally, a 4-sided kite can also be chosen, shown as (3); as in (2), the deformations can be chosen to prevent any modification to the corners.

S2 SDA Tile Summary

Figure S6 contains the summary of all tiles simulated in this work, their edges, and associated symmetry group.

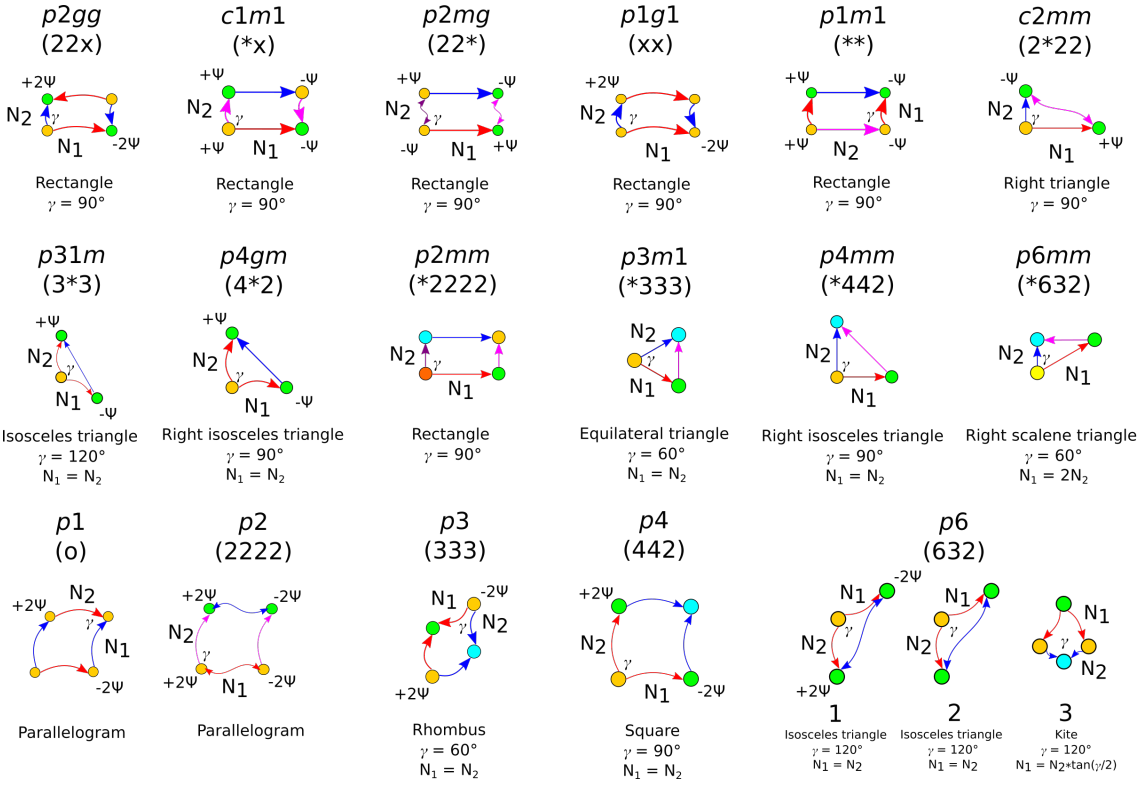

Figure S6: Summary of the shapes of SDAs simulated in this work. A geometric description accompanies each tile illustrating the length of each side, deformations made, and any restrictions. Again, identically colored spheres denote symmetrically identical corners; symmetrically equivalent edges are denoted by the color and the direction of their arrows. There is no connection between the colors of the corners and the edges.

S3 Model Details

S3.1 Bond Stretching

Rings are deformed by bending their edges consistent with the isometry that operates on them as described in the main text. This encompasses the cases where: (1) an edge may be reflected, (2) it may be translated (possibly after also being reflected) or rotated about a corner to match a different edge on the ring, or (3) it may contain a two-fold rotation center at its midpoint. Note that two-fold rotation centers are always located at the midpoints of edges if they are not located at vertices, as required by symmetry. [1]

Edges along which a reflection occurs are required to remain undeformed (straight); deformations only occur for the other two cases. These edges of rings are deformed by imagining a circle is inscribed between its two ends in the case of a "translated" (T) edge (case 2), or by a pair of identical circles in contact when there is two-fold center of rotation (R) at its midpoint (case 3) as depicted in Figs. S7(b,c), respectively. These deformations respect the symmetry elements themselves and make edges operated on by different isometries distinguishable from each other. By electing this method of deformation, the ring's equilibrium angles along its edges and corners may be expressed purely as a function of the perturbation angle, ψ, defined as the change in the angle at the corners (vertices) of the chosen fundamental domain.

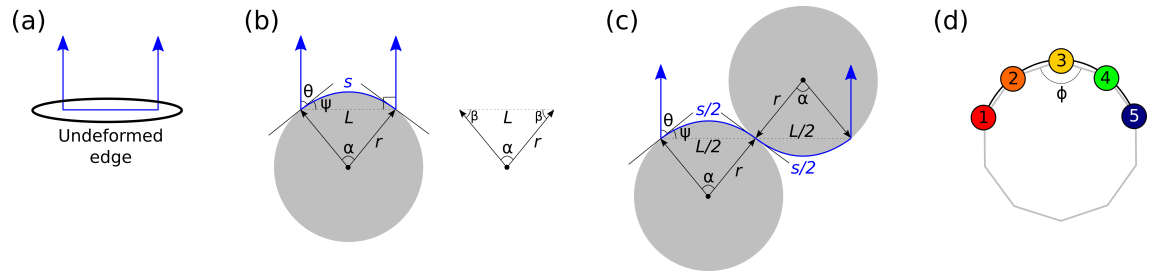

Figure S7: Deformation of a fundamental domain's edge. (a) The undeformed edge as a reference is given with two orthogonal rays at each end. These rays do not correspond to other edges on the domain, but are simply fictitious constructs required in the derivation. (b) Deformation of a "translated" edge (T case) by inscribing a circle (gray) of radius, r. This causes a deflection at the endpoints of angle ψ. The triangle at the right defines the angle β. (c) Deformation of an edge with a two-fold rotation center (R case) at its midpoint by two equally sized circles of radius, r. For consistency with (b) the total linear distance between endpoints is described as L. (d) Illustration of a regular polygon whose vertices are given by the beads along an edge, with equilibrium angle ϕ.

In our model, we elect to use a single ψ to characterize all edges on a fundamental domain, along which we placed a discrete number of beads; however, since some fundamental domains form triangles, for example, the length of some edges will necessarily not correspond to an integer number of beads. Moreover, some wallpaper groups allow the relative lengths of our choices of edges to vary and thus if one is of integer length, others will not be. [2, 3] The number of beads required along such edges is computed by rounding down, $N = \lfloor L/\sigma \rfloor$, where N is the number of beads (with a diameter of σ) to be placed on the edge of length, L. To accommodate this discrete nature of the model, the bonds between the beads must be allowed to stretch so that when extended, the edge in question can reach the desired length. Since edges made of an integer number of beads do not need to stretch at all, the amount of required stretching will vary within the ring. Rather than specify stiff bonds of different equilibrium lengths, we chose to allow all bonds to stretch up to the maximum extent required by any edge that is not an integer number of beads in length.

First we derive this bond stretching factor for the T case. In this instance, the linear distance, L, between and edge's endpoints should remain unchanged to be consistent with the desired wallpaper group's geometry. Since our model is composed of discrete beads, they will have to be placed along the arc which has length, s, and thus, relative to the unperturbed case, will require that their bonds be allowed to stretch farther. This stretching factor is simply given by $F_{\mathrm{T}}\sigma = s/(N-1) = (s/L) * (L/(N-1))$, where there are to be N beads (and therefore $N-1$ bonds) placed along the edge inclusive of the endpoints. The arc length follows directly from $s = r\alpha$, where r is the radius of the inscribing circle and α is the angle as shown in Fig. S7(b). However, α is unknown and we instead seek an expression in terms of ψ.

Since θ is defined with respect to the surface tangent, $\pi/2 = \beta + \psi$, and $\pi/2 = \theta + \psi$, so $\beta = \theta$; combined with the Law of Sines we have:

$$\frac{\sin\,\alpha}{L} = \frac{\sin\,\beta}{r} = \frac{\sin\,\theta}{r}. \tag{1}$$

Rearrangement yields:

$$\frac{s}{L} = \frac{r\alpha}{L} = \alpha\left(\frac{\sin\,\theta}{\sin\,\alpha}\right). \tag{2}$$

Inserting $\theta = \pi/2 - \psi$, and $\alpha = \pi - 2\beta = \pi - 2\theta = \pi - 2(\pi/2 - \psi) = 2\psi$ we arrive at

$$\begin{aligned} F_{\mathrm{T}}\sigma &= \alpha\left[\frac{\sin(\pi/2-\psi)}{\sin\,\alpha}\right]\left[\frac{L}{N-1}\right] \\ &= 2\psi\left[\frac{\sin(\pi/2-\psi)}{\sin(2\psi)}\right]\left(\frac{L}{N-1}\right). \end{aligned} \tag{3}$$

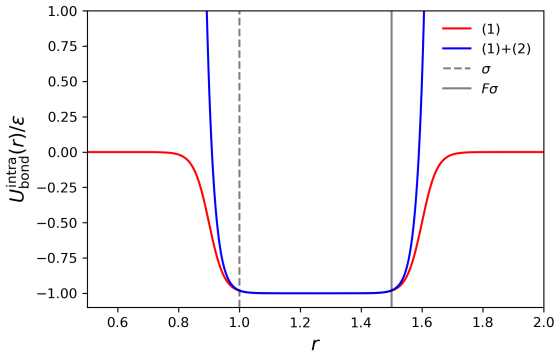

Figure S8: Illustration of the bonding potential used in our simulations. More details are available in the Sec. 2 (Methods) of the main text.

Note that when $\psi = 0$ (no perturbation or bending), we have an indeterminate expression $F_{\text{T}} \sim 0/\sin(0) = 0/0$; however, from L'Hospital's rule we have a well-defined limit:

$$\lim_{\psi\to 0} F_{\text{T}}\sigma = \lim_{\psi\to 0}\left(\frac{L}{N-1}\right)\left[\frac{\sin(\pi/2-\psi)-\psi\cos(\pi/2-\psi)}{\cos(2\psi)}\right] = \frac{L}{N-1}, \tag{4}$$

i.e., $s/L \to 1$, as expected, though this limit must be explicitly programmed. Note that mirror edges are never deformed and thus always have $s/L = 1$ ($\psi = 0$). Also note the upper bound for the validity of this expression is when the sphere has "fully impacted" the edge, making its equator lie along the original straight line (diameter $= L$); in this case, $\psi = \pi/2$, and the above expression reveals, as expected, $s/L \to \pi/2$.

After inspection of Fig. S7(c) it is clear that the above expression holds for the R case as well, assuming that once again, θ is defined as the angle formed with a ring's corner as its vertex. In this case, two circles are assumed to be inscribed between the endpoints (as shown) meeting at the midpoint where the 2-fold rotation center is. Following the same steps, we arrive at $F_{\text{R}} = F_{\text{T}}$, where L always refers to the linear distance between the two endpoints and N is the total number of beads to be placed between them. Figure S8 illustrates the bonding potential, as described further in the main text. This shows how the bond stretching factor determines the width of the potential's well.

S3.2 Additional Simulation Details

The fractional surface coverage, f, of a system was computed as:

$$f = \frac{N_{\text{tot}} A_{\text{ring}}}{A}, \tag{5}$$

where A is the total area of the two dimensional simulation cell, N_{tot} is the number of rings present, and A_{ring} is the estimated surface area of a ring. This surface area is computed assuming the ring has adopted is ideal (target) conformation and is undeformed, as given in Figs. S1–S5. This is computed as:

$$A_{\text{ring}} = \text{abs}\left[\det\begin{vmatrix} N_2\cos\,\gamma & N_2\sin\,\gamma \\ N_1 & 0 \end{vmatrix}\right], \tag{6}$$

where "abs" denotes the absolute value, N_1 and N_2 are the number of beads placed along adjacent edges of the domain, and γ is the interior angle. This determinant yields the area of the parallelogram defined by these vectors; however, some domains are triangular, and are actually formed by dividing this parallelogram in half, *e.g.*, all groups in row 3 (*cf.* Fig. S3). In this case, $A_{\text{ring}} \to A_{\text{ring}}/2$.

S4 Scoring Function

We scored the degree of correct assembly in a system by looking at all interacting pairs of rings. For each ring, we defined a vector along each edge and compared how these vectors were oriented relative to each other

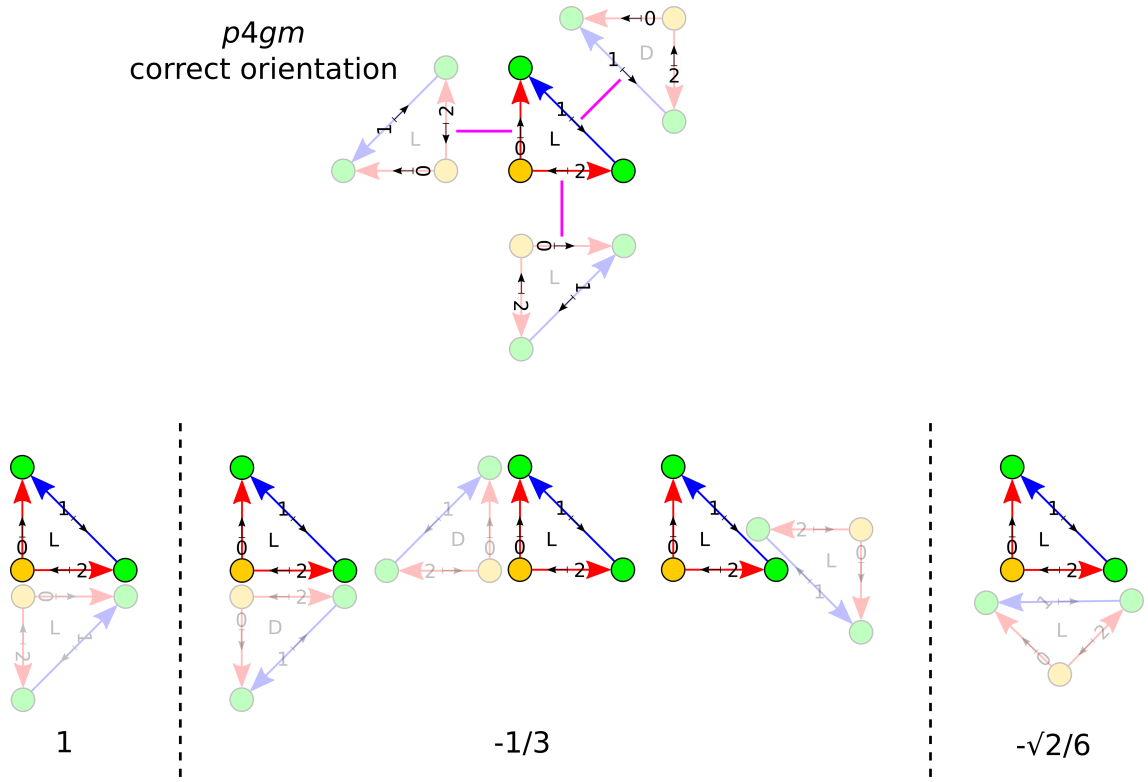

Figure S9: Orientations of *p4gm* fundamental domains. At the top, the ideal orientation around a domain of chirality L. Edges are numbered and the black vectors denote the handedness; the colored arrows merely denote the underlying symmetry as given in Fig. S3. The approaching domain (ring B) is always depicted as transparent. At the bottom, three characteristic types of relative orientations are shown along with their scores, $S_{\mathrm{A,B}}$.

versus how they should be in an ideal scenario. To compute these vectors, the vector between the centers of mass of beads n and $n+1$ were computed for all beads along a ring's edge; the mean vector was taken and assumed to be at the edge's center of mass. Note that the chirality of the ring determines the direction the beads were created in, meaning the vector simply points in the opposite direction for otherwise identical rings of different chiralities. For example, in Fig. S10 rings of different chiralities are indicated by different colors (blue or orange) and the vectors along their edges are pointing in a right-handed, counterclockwise fashion in the former, and in a left-handed, clockwise fashion in the latter.

A ring "A" that interacts with another ring "B" across a given edge of A determines the expected orientation of each of the vectors along the edges of B. For example, in Fig. S9, the ideal orientations around one enantiomorph (called "L") corresponding to ring A are shown for the *p4gm* group; its yellow corner is a 4-fold rotation center, therefore ring B should be an L enantiomorph across both (red) edges 0 and 2. The blue edge (edge 1) is a mirror plane so the other enantiomorph, "D", is expected. Clearly, expectations are different for different edges. Therefore, we can define an expected angle, $\theta_i(j)$, that the vector along edge i on ring A should be rotated counterclockwise so that it matches its orientation on ring B, when B is correctly oriented across edge j of ring A. Even if ring B is placed incorrectly, it is possible that some its edges are aligned as expected but not others.

In Fig. S9 three different examples of different characteristic orientations and their scores are given. First, in the ideal case, $S_{A,B} = s_{A,B} = s_{B,A} = 1$ when another L enantiomorph aligns its edge 0 with ring A's edge 2; *e.g.*, rings 4 and 26 in Fig. S10. By contrast, if a D enantiomorph approached in such a way that one of its red edges matched one on ring A, then $S_{A,B} = s_{A,B} = s_{B,A} = -1/3$; *e.g.*, rings 3 and 6 in Fig. S10. The same score results if another L enantiomorph makes contact with ring A's blue edge. Finally, if another L enantiomorph happens to approach so that its edge 1 contacts ring A's edge 2, then $s_{A,B} = -\sqrt{2}/2$, while

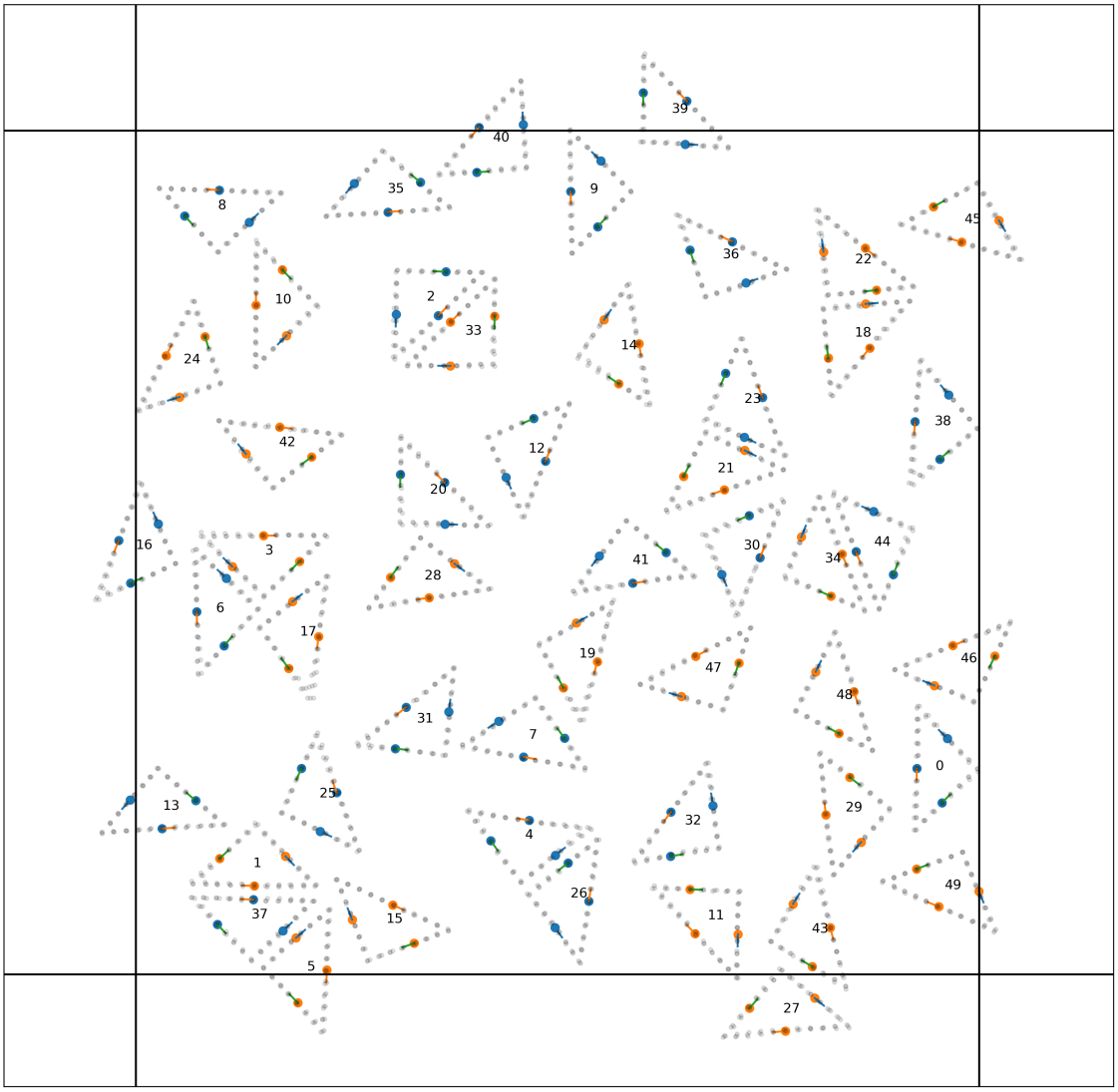

Figure S10: A snapshot from a simulation of a racemic mixture of *p4gm* rings. The box is indicated by thick black lines, and rings which go past an edge have had their coordinates unwrapped. The vectors along the edges of each ring are given by a different color starting from the edge's center of mass; these centers are colored blue or orange to indicate different enantiomorphs. Gray points indicate the locations of the beads of the ring. The index of each ring is depicted at the center of the ring.

$s_{B,A} = +\sqrt{2}/6$ so that $S_{A,B} = -\sqrt{2}/6$.

In the main text, we defined the global score for a system based on these pairwise interactions as:

$$S = \langle N_{\mathrm{n}} \rangle \langle S_{A,B} \rangle, \tag{7}$$

where $\langle N_{\mathrm{n}} \rangle$ is the average number of interacting neighbors a ring has, and $\langle S_{A,B} \rangle$ is the average score of interacting pairs of rings. This score reflects the product of the (1) local densification or aggregation of rings, and (2) the degree of their local alignment. If each edge only interacts with a single ring, N_{n} is bounded above by N_{e} (defined in main text); however, it is possible that multiple rings could be in contact with the same edge, so in principle N_{n} is bounded by local packing constraints around ring A. The pairwise score is bounded $-1 \leq S_{A,B} \leq +1$. First, note that S, like $S_{A,B}$, is not necessarily monotonic in pairwise energy. In Fig. S9 the orientations with $S_{A,B} = -1/3$ have 1 edge aligned and therefore an energetic benefit ($E < 0$), whereas when $S_{A,B} = -\sqrt{2}/6 > -1/3$, there are no matches and so $E = 0$. However, when local defects are present, they generally destroy long range order; the more aligned a system is ($\langle S_{A,B} \rangle \to 1$), the lower the total energy of the system can be.

S5 Simulation Results

In Figs. S11–S16, the first three graphs illustrate the global score, S, and its individual components for the three representative cases of: (1) a single chirality system of undeformed rings, (2) a racemic mixture of undeformed rings, and (3) and racemic mixture of deformed rings. Generally, the deformation angle was set to $\psi = 15°$, unless otherwise stated. Snapshots of the last frame in these simulations are shown at the right, outlined in the color corresponding to the score curves: blue, orange, and green for cases (1), (2), and (3), respectively. The upper snapshot is of the rings themselves colored according to chirality (red or blue, arbitrary), while the lower image is colored according to $S_{A,B}$ divided into 5 bins as illustrated by the colorbar at the right. Cartoons of the undeformed rings are included as insets for reference.

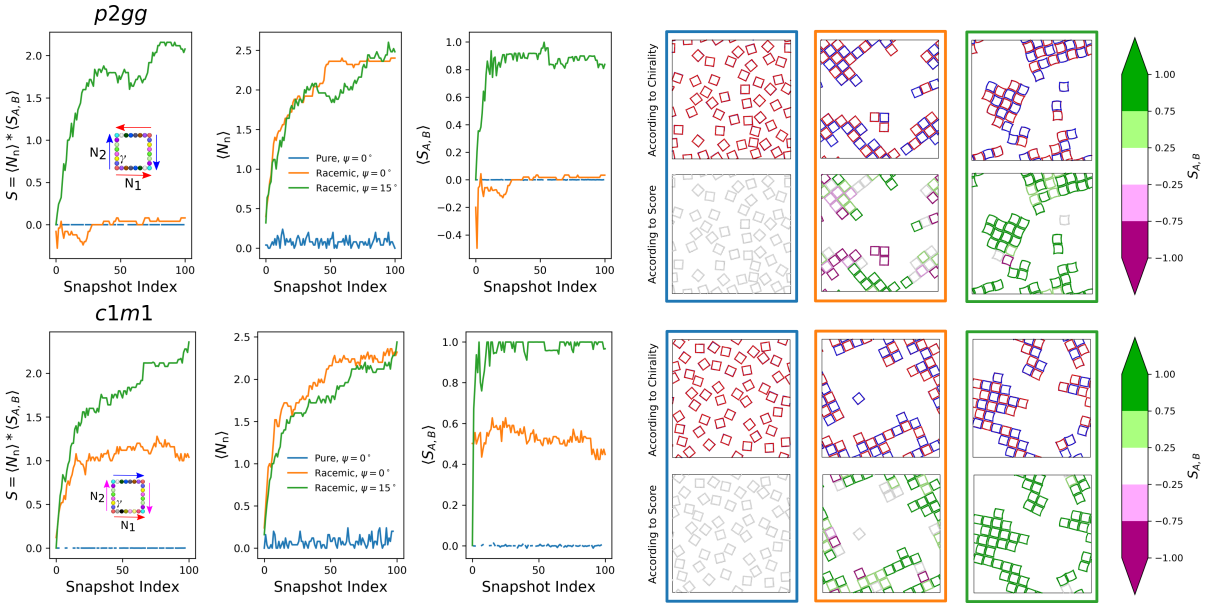

Figure S11: Row 1 simulation results. The boundaries of these rings are formed by exclusively using symmetry operations that include reflections (including glides which are a combination of reflection and translation) and as a result, each ring must be surrounded on all sides by the opposite chirality. Thus, single chirality systems do not assemble at all (*cf.* blue curves and boxes); strictly speaking, at sufficiently low T^* single beads from different rings may align, leading to a disordered aggregate (*cf.* main text). Racemic mixtures, can assemble, however, the relative orientation of a ring's neighbors is not guaranteed; thus while the number of neighbors each ring has, $\langle N_\mathrm{n} \rangle$, rises, the average pairwise score of each interaction remains essentially random (*cf.* orange curves and boxes). When the rings are deformed ($\psi = 15°$) this is remedied and $\langle N_\mathrm{n} \rangle$ is about the same as in the undeformed, racemic mixture, but now $\langle S_{A,B} \rangle \to 1$ (*cf.* green curves and boxes).

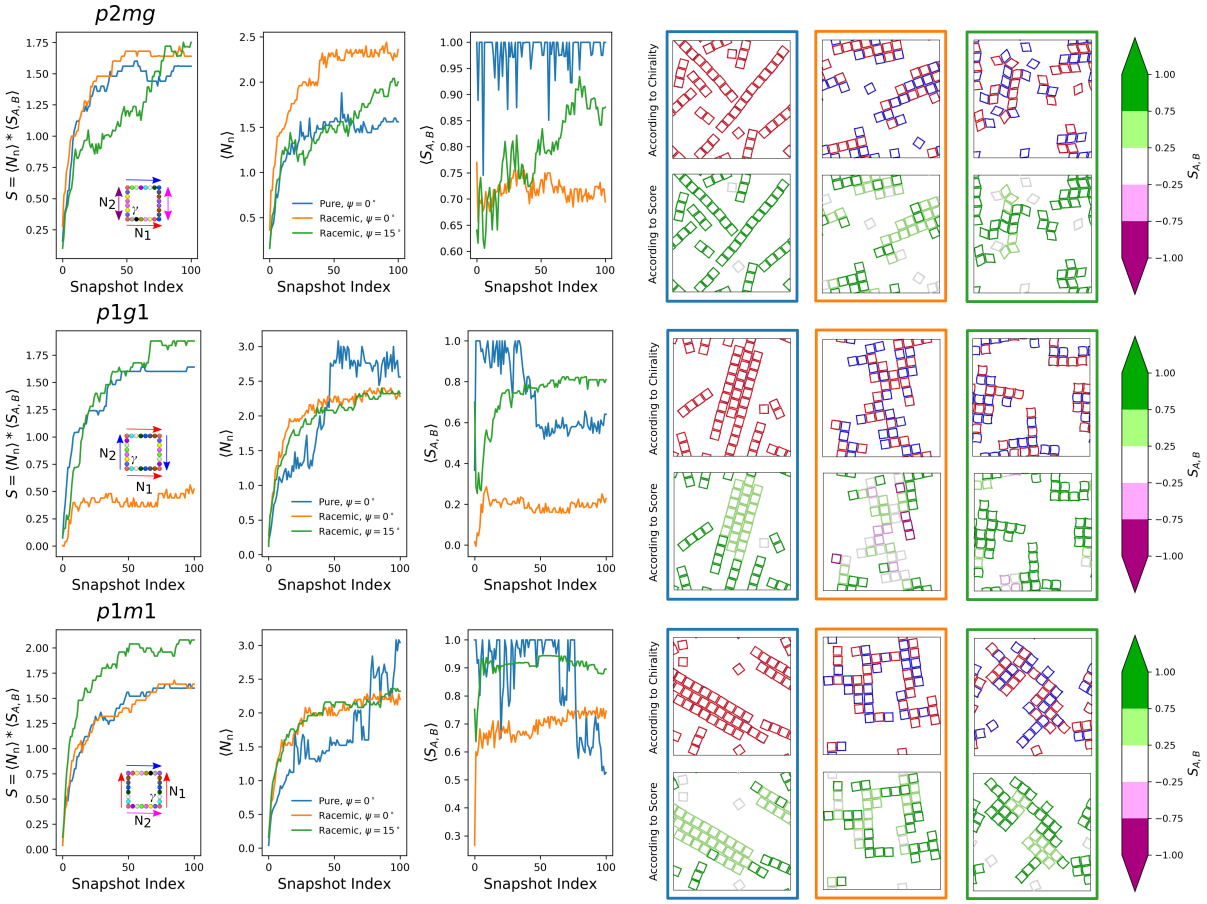

Figure S12: Row 2 simulation results. The boundaries of these rings contain a single set of opposing edges that result from symmetry operations involving reflections (including glides which are a combination of reflection and translation); thus, rings of the opposite chirality are required to enable assembly along those edges. The other edges can be "matched" by rings of the same chirality. The result is that for single chirality systems assembly is suppressed in one direction but enabled in the other, resulting in "1D strings" (*cf.* blue curves and boxes). A racemic mixture of undeformed rings can assemble in all directions, but the relative orientation of neighbors is not guaranteed resulting in defects (*cf.* orange curves and boxes). Once deformations ($\psi = 15°$) are introduced, this is remedied (*cf.* green curves and boxes). Notably, the single chirality case is subject to aggregation of strings driven by interactions of single beads along the non-assembling edge; the result is a rapid increase or decrease in $\langle N_\mathrm{n} \rangle$ complemented by changes in $\langle S_{A,B} \rangle$ as illustrated in the $p1m1$ and $p1g1$ examples. Note that the results for $p1g1$ were obtained at a slightly lower $T^* = 0.3$.

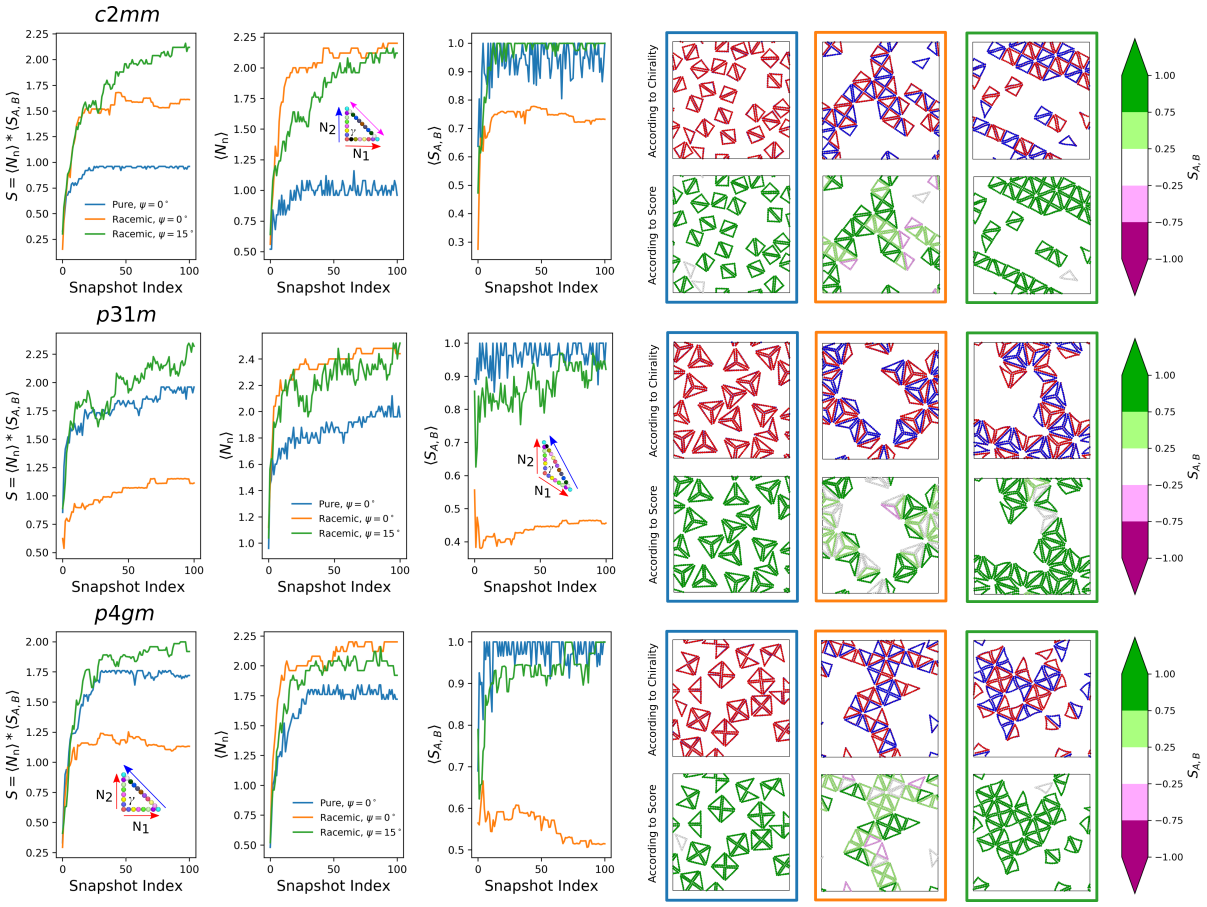

Figure S13: Row 3 simulation results. The orbifold symbol for these groups is of the form A*{b} where A is an integer and {b} is a non-empty set of integers. This indicates the presence intersecting mirror planes (denoted by {b}) with a center of rotation (denoted by A); specifically A = 2, 3, or 4 for $c2mm$, $p31m$, and $p4gm$, respectively. Since a ring requires another ring of the opposite chirality across a mirrored edge, the intersecting mirror planes effectively form a concave "shell" enclosing a set of fundamental domains. The order of the interior rotation determines how many. Consequently, single chirality systems form nearly perfect ($\langle S_{A,B} \rangle \to 1$) dimers (A = 2), trimers (A = 3), or tetramers (A = 4) as shown by the blue curves and in the blue boxes. An undeformed, racemic mixture can assemble in all directions increasing $\langle N_\mathrm{n} \rangle$, but again, the relative orientations of different rings are not guaranteed meaning $\langle S_{A,B} \rangle$ is very low (*cf.* orange curves and boxes); this is opposite the single chirality case (*cf.* blue curves and boxes). By deforming the edges ($\psi = 15°$) the best of both worlds may be achieved resulting in a high global S (*cf.* green curves and boxes).

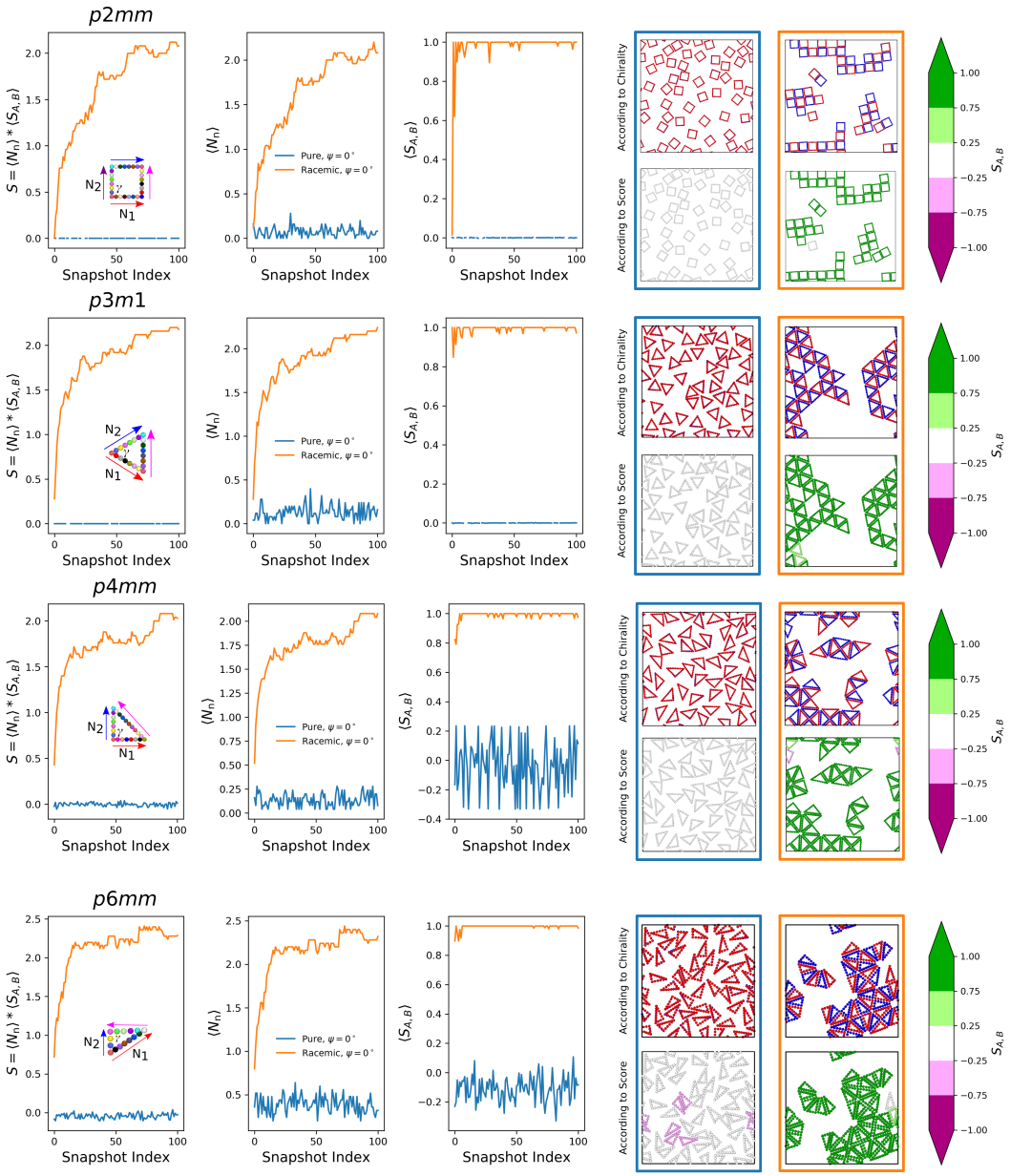

Figure S14: Row 4 simulation results. The orbifold symbol for these groups is of the form *{a} where {a} is a non-empty set of integers. This indicates the exclusive presence of intersecting mirror planes that make angles denoted by {a}; for example, the fundamental domain for $p6mm$ (*632) is a triangle generated by 3 intersecting mirror planes making angles of $\pi/6$, $\pi/3$, and $\pi/2$. Reflections are the only symmetry operation involved in these groups, and as a result, each ring must be surrounded by its opposite chirality on all sides to assemble; single chirality systems, therefore, do not assemble at all ($\langle S_{A,B} \rangle \to 0$), whereas racemic mixtures tend to assemble perfectly ($\langle S_{A,B} \rangle \to 1$) as shown in blue and orange, respectively. Since all edges are mirrors, all edges are straight and no deformations are permitted. Here, due to its smaller size, the $p6mm$ ring required a slightly lower $T^* = 0.2$ to assemble.

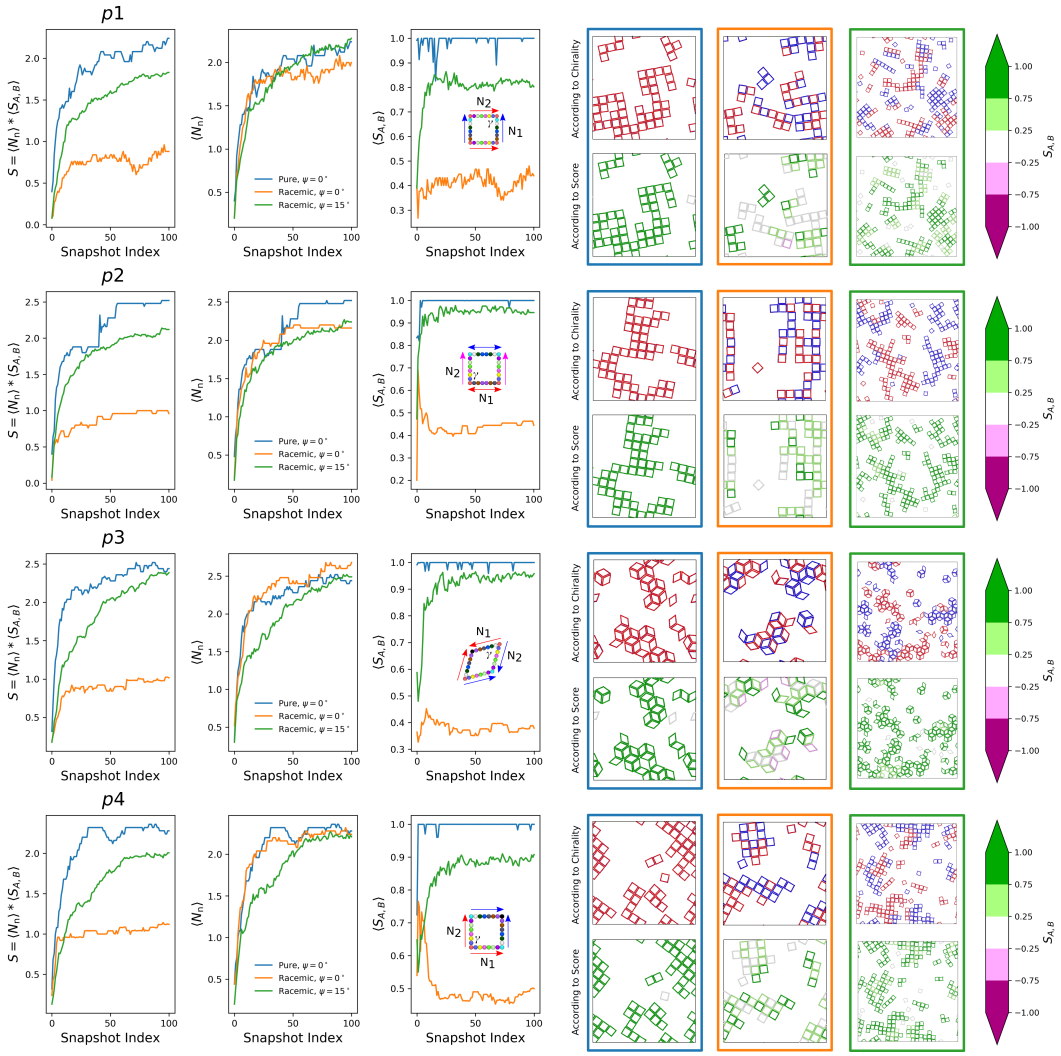

Figure S15: Row 5 simulation results ($p1$–$p4$). The orbifold symbol for these groups is of the form {A} where {A} is a non-empty set of integers. This denotes the presence of rotation centers with orders given by A; for example, $p3$ (333) is generated by the combination of three 3-fold centers of rotation. No symmetry operations besides rotations are present. The exception being $p1$ (o) where there are no rotations. Due to the absence of reflections, single chirality systems are actually ideal and can assemble without defect (*cf.* blue curves and boxes, $\langle S_{A,B} \rangle \to 1$). Racemic (undeformed) mixtures, in principle could assemble perfectly well if the two enantiomorphs were kept separate, however, in practice they are free to intermingle and form defective structures with the same average number of neighbors as the single chirality case (*cf.* orange curves). This can be remedied by introducing deformations ($\psi = 15°$) to the rings; this results in phase-separated regions of each chirality. Naturally, these domains make contact forming an interface which is perceived as a defect. To illustrate these domains better, here we show the racemic, deformed results for $N = 200$ rings instead of $N = 50$. Note that $p6$ is also a member of this row, but is examined in more depth in Fig. S16.

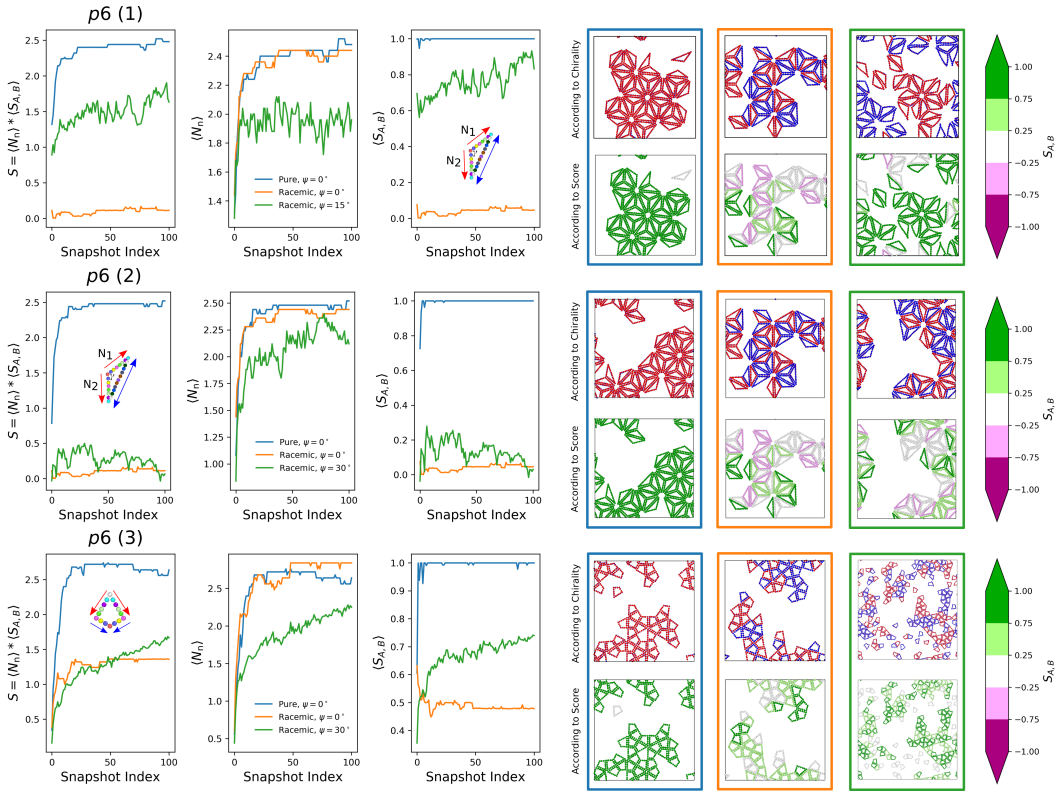

Figure S16: Simulation results for the group $p6$. This group also belongs to row 5 and its rings (fundamental domains) exhibit behavior identical to those of other groups found in this row. Here, we illustrate several different possible choices for the ring, as given in Fig. S5. In the first case, the ring is formed by taking an isosceles triangle and making one acute corner more acute and the other more obtuse. The second case results from simply "twisting" the triangle's edges without requiring a deformation of the corner angles. The difference results from placing the "sine wave" (corresponding to the deformation associated with the 2-fold rotation center along the hypotenuse) in different directions relative to the deformations made on the other two edges. Finally, we can also form a 4-sided kite as in case (3). For all these rings, the single chirality case assembles perfectly ($\langle S_{A,B} \rangle \to 1$) as shown in blue; while the racemic, undeformed mixtures assemble defectively. In principle the choice of the ring does not matter, however, from a practical perspective certain angles can make structures easier or harder to assemble based on packing of the spheres (circles) out of which the rings are composed. Choice (3) was found to be more robust for large systems [$N = 200$ for case (3)], though over the same amount of simulation time as the other cases [$N = 50$ for cases (1) and (2)] the system did not fully anneal (*cf.* green curves); regardless, the linear trend of S suggests it will continue over time. Note that the shorter edges of the ring in (3) required a lower $T^* = 0.2$ and larger $\psi = 30°$ to assemble. This size was chosen so that the unit cell of the crystal would be approximately the same across all cases and does not qualitatively affect any conclusions.

References

[1] *International Tables for Crystallography Volume A: Space-group Symmetry.* International Union of Crystallography, 1983.

[2] N. A. Mahynski, E. Pretti, V. K. Shen, and J. Mittal, "Using symmetry to elucidate the importance of stoichiometry in colloidal crystal assembly," *Nature Communications*, vol. 10, p. 2028, 2019.

[3] E. Pretti, V. K. Shen, J. Mittal, and N. A. Mahynski, "Symmetry-based crystal structure enumeration in two dimensions," *The Journal of Physical Chemistry A*, vol. 124, pp. 3276–3285, 2020.

[4] R. Fricke and F. Klein, "Vorlesungen über die theorie der automorphen funktionen. band 1: Die gruppentheoretischen grundlagen. band ii: Die funktionentheoretischen ausführungen und die andwendungen," *Bibliotheca Mathematica Teubneriana, Bände*, vol. 3, no. 4, 1965.

[5] L. Keen *et al.*, "Canonical polygons for finitely generated fuchsian groups," *Acta Mathematica*, vol. 115, pp. 1–16, 1966.

[6] A. Macbeath, "Generic dirichlet polygons and the modular group," *Glasgow Mathematical Journal*, vol. 27, pp. 129–141, 1985.

[7] B. Grünbaum and G. C. Shepherd, "Tilings and patterns," 2016.

[8] C. K. Johnson, M. N. Burnett, and W. D. Dunbar, "Crystallographic topology and its applications," *Crystallographic Computing*, vol. 7, pp. 1–25, 1996.